



Label-free ultra-sensitive visualization of structure below the diffraction resolution limit

Title	Label-free ultra-sensitive visualization of structure below the diffraction resolution limit
Author(s)	Alexandrov, Sergey;McGrath, James;Sheppard, Colin J. R.;Boccafroschi, Francesca;Giannini, Cinzia;Sibillano, Teresa;Subhash, Hrebesh;Hogan, Josh;Leahy, Martin
Publication Date	2018-03-23
Publisher	Wiley
Repository DOI	10.1002/jbio.201700385

FULL ARTICLE

Label-free ultra-sensitive visualization of structure below the diffraction resolution limit

Sergey Alexandrov^{1*} | James McGrath¹ | Colin J. R. Sheppard² | Francesca Boccafroschi³ | Cinzia Giannini⁴ | Teresa Sibillano⁴ | Hrebesh Subhash⁵ | Josh Hogan⁶ | Martin Leahy¹

¹Tissue Optics & Microcirculation Imaging Group, School of Physics, National University of Ireland, Galway, Ireland

²Department of Nanophysics, Istituto Italiano di Tecnologia, Genoa, Italy

³Department of Health Sciences, University of Piemonte Orientale "A. Avogadro", Novara, Italy

⁴Institute of Crystallography, National Research Council, Bari, Italy

⁵Colgate-Palmolive Global Technology Center, Piscataway, New Jersey

⁶Compact Imaging, Mountain View, California

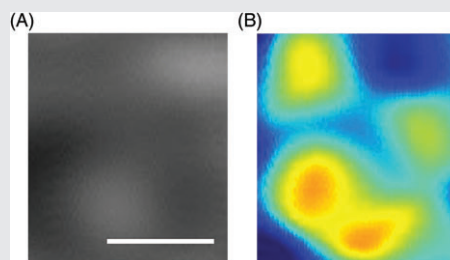
***Correspondence**

Sergey Alexandrov, Tissue Optics & Microcirculation Imaging Group, School of Physics, National University of Ireland, Galway, Ireland.
Email: serгей.alexandrov@nuigalway.ie

Funding information

Compact Imaging; Irish Government and the European Union; Higher Education Authority PRTL Cycle 4; National Biophotonics Imaging Platform (NBIP) Ireland; University of Limerick Foundation; Galway University Foundation; NUI Galway

For both fundamental study of biological processes and early diagnosis of diseases, information about nanoscale changes in tissue and cell structure is crucial. Nowadays, almost all currently known nanoscopy methods rely upon the contrast created by fluorescent stains attached to the object or molecule of interest. This causes limitations due to the impact of the label on the object and its environment, as well as its applicability in vivo, particularly in humans. In this paper, a new label-free approach to visualize small structure with nano-sensitivity to structural alterations is introduced. Numerically synthesized profiles of the axial spatial frequencies are used to probe the structure within areas whose size can be beyond the diffraction resolution limit. Thereafter, nanoscale structural alterations within such areas can be visualized and objects, including biological ones, can be investigated with sub-wavelength resolution, in vivo, in their natural environment. Some preliminary results, including numerical simulations and experiments, which demonstrate the nano-sensitivity and super-resolution ability of our approach, are presented.



KEYWORDS

label-free imaging, nanoscale sensitivity, optical microscopy, sub-micron structure, super-resolution

1 | INTRODUCTION

The importance of high resolution imaging has been acknowledged by the award of the Nobel Prize for Chemistry in 2014. Using super-resolution images should reveal very interesting and innovative diagnostic solutions in assessing the health of the tissue, and early identifying traits of a specific disease or damage. For instance, research is exploring more and more sophisticated techniques able to distinguish healthy and cancerous tissues, depending on collagen fiber changes (ie, breast cancer), thus, indicating

collagen as a potential cancer diagnostic parameter. Besides the development of the label-based techniques, some label-free methods to improve resolution beyond the diffraction resolution limit of an optical system, or below the ultimate resolution limit, have been published [1–9]. In some cases, to detect pathological areas or small structural changes in time, it is more important to provide high sensitivity to structural changes than high spatial resolution. Corresponding phase microscopy techniques have been proposed to detect sub-diffractive refractive index fluctuations [10–16]. A recently proposed approach, spectral encoding

of spatial frequency (SESF) imaging, was developed for visualization of internal structure with nano-sensitivity to structural changes [17–19]. This approach has been adapted for depth-resolved imaging [20, 21] and for super-resolution imaging [22].

According to the information theory treatment of optical imaging, it is not the resolution itself that is an invariant for a particular optical system, but rather the capacity for information transfer through the system [23–25]. Then resolution can be improved by trading off some other property, for example signal-to-noise ratio [25], or axial image information [25], or spectral information [26–28]. In our case at each image point we do not just have a single intensity value, but an axial spatial frequency profile [19, 20], so it could be hundreds or even thousands values.

A normally incident plane wave, when back-scattered by a sample, is scattered by a grating vector with spatial frequency twice that of the wave vector. The resulting inverse relationship between spatial frequency and optical wavelength is the basis of conventional reconstruction in white light interferometry or optical coherence tomography (OCT) [29, 30]. However, for illumination with a range of incident angles it is only an approximation, as a transverse spatial frequency results in a decrease of axial spatial frequency. A result of this effect is that interference fringe spacing changes with angle of incidence [31]. Improved OCT reconstruction algorithms, valid for higher numerical apertures, have been developed [32, 33].

In this paper we propose a new version of the SESF approach, with potentially sub-nano sensitivity and sub-wavelength spatial resolution, for visualization, comparison and quantitative estimation of structure within an object or of different objects.

2 | METHODS AND MATERIALS

2.1 | Method

The basic theory of the SESF approach has already been published [20]. Different aspects of the SESF approach were also published in a number of journals [17–19]. Briefly, the structural characteristics of any 3D object can be rigorously described by its Fourier transform, a distribution of its spatial frequencies. From general scattering theory it is known that if sample is illuminated by broadband plane wave, then all accessible spatial frequencies of the object's structure can be represented in K -space as a number of Ewald spheres, where each wavelength corresponds to 1 sphere [34]. In reflection—mode configuration at normal incidence the frequency vector K forms the NA-restricted Ewald sphere caps, where NA is a numerical aperture of the imaging system. A succession of Ewald sphere caps defines a muffin-shaped region of spatial frequency support in K -space for reflection geometry. For given wavelength

and known illumination/detection geometry and refractive index the corresponding spatial frequencies can be calculated. In reflection configuration the accessible spatial frequencies provide information about small, submicron structure and highly sensitive to structural changes. It was shown that for moderate NA, the axial spatial frequency, corresponding to the NA-restricted Ewald sphere cap and defined by a single wavelength, is weakly dependent on the back-scattering angle. As a result, each axial spatial frequency (axial spatial period) can be encoded by a unique wavelength (corresponding to a single NA-restricted Ewald sphere cap) with a small uncertainty [18, 20]. It means that the wavelengths can work as vehicles to pass the spatial information about small sub-micron structure of the object through the imaging system independently on NA. If spectrum is detected for each image point, for example, using imaging spectrometer, then it is possible to convert such spectrums into the axial spatial frequency/periods profiles using simple formulas (see, for example, formula (22) in [20]). Thus the axial spatial frequency profiles, which are extremely sensitive to structural alterations, can be reconstructed for each image point, as shown in Figure 1A,B. The distances between points, where these profiles are reconstructed, can be shorter than the resolution limit of the imaging system. Then an image can be formed as a color map of some informative parameters of this spectrum, for example, as a map of the spatial frequency or period at maximal signal, the mean spatial frequency, or the correlation coefficient between axial spatial frequency profiles at a given point and profiles at all other points within the image.

The SESF approach is clearly distinct from phase-based microscopic imaging approaches [10–16], both in its physical basis and the result. In phase microscopy, the phase difference which relates to optical path length difference (integrated along the whole depth) is detected at each image point. The SESF approach facilitates detection of spatial frequency components of the structure along the optical path length and hence the structural sizes within the sample. In contrast to phase microscopy, at each image point we have information about many spatial frequency components, that is, axial spatial frequency profiles. Thus, the information content of the SESF images is dramatically improved, beyond traditional phase microscopy, which permits improved sensitivity and formation of super-resolution images. The SESF approach is a non-interferometric approach whereas almost all known phase microscopy techniques are based on interferometry. The approach is not sensitive to displacements, only to structural changes, and so is more stable than phase-based methods, for example in live imaging. Several objects could look the same as 1 object with the same cumulative size and refractive index in phase microscopy but, in SESF, would be detected as different axial frequency profiles related to the physical sizes of the structures therein. Therefore SESF microscopy, having

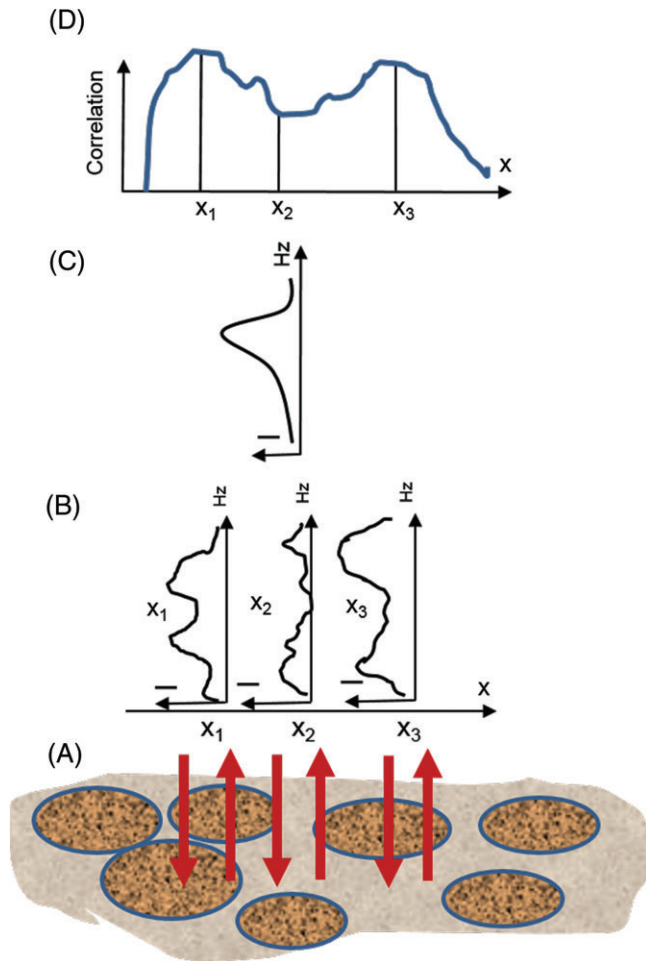


FIGURE 1 Schematic diagram of the image formation process: (A) the object, (B) the reconstructed axial spatial period profiles, (C) the profile of the numerically synthesized structure, (D) the sSESF image

obvious advantages, could be also a good complementary technique to phase-based microscopy.

Our novel contrast mechanism sSESF, presented here, is based on comparison of the axial spatial frequency or period profiles, reconstructed for each image point Figure 1B, with the profile of a numerically synthesized structure Figure 1C. The images are formed as maps of corresponding correlation coefficients, as in Figure 1D.

Using our approach it is possible to estimate how the structure within different areas of the sample is close to the probing structure and visualize areas in the sample which has the structure similar to probing structure. For example, if the correlation coefficient is constant along the image, it means that the structure within the sample is uniform, nothing to resolve. The variations of the correlation coefficient along the sample visualize the difference in structure at different locations. The values of the correlation coefficient at different locations provide quantitative information about how close the structure at given location to probing structure. So the sSESF images are much more informative than conventional images. We will show that the sizes of areas within the sample with different structure could be even

smaller than the resolution limit of the imaging system. Thus using sSESF approach it could be possible to visualize and locate, for example, the pathological areas within the sample.

It is also possible to perform comparison of the structure of different samples. In this case, the numerically synthesized structure can be considered as a reference structure, and so it is possible to investigate how the structure of samples is different from the reference structure.

The probing structure can be generated numerically or axial spatial frequency profile of real structure can be used (eg, the profile of some structure with pathological changes, say cancered tissue, to select pathological areas within the other samples).

sSESF approach also permits to form super-resolution images. Really, in conventional intensity-based images at each image point just 1 intensity value of scattered wave is detected. This scattered wave is a superposition of light waves scattered on different constituents within the sample along the depth. Even thin samples for microscopic study with thickness of about $4\mu\text{m}$ usually have at least a few scatterers along the depth at each lateral point. If the distance between 2 features in the sample, separated in lateral directions, is smaller than the resolution limit of the imaging system, then the difference in intensities at these features and at spacing between them became undetectable and it is not possible to resolve them. But, in contrast to conventional microscopy, using SESF approach at each image point we detect not just 1 value, but axial spatial frequency profiles, many values. So information content of the image is dramatically improved. Instead of comparison intensity values we compare axial spatial frequency profiles at features within the sample and axial spatial frequency profile of the numerically synthesized structure, so we use many values at each image point for comparison. As a result the features which cannot be resolved using conventional microscopy can be resolved using our approach. To test our approach we performed both a numerical simulation of the imaging process and experiments.

2.2 | Numerical simulation

The samples with different structure were numerically synthesized to demonstrate different aspects of our approach. First of all, the sample which consists of 2 areas with different axial structure was generated to confirm high sensitivity of the sSESF approach to structural alterations. This sample is presented in Figure 2A where 2 areas are shown in different colors, green and brown. There are 10 equally separated scatterers at each point within the areas in the depth direction. For structure within 2 brown lines this separation is 449.9 nm and for structure within other area this separation is 450 nm . So the difference in axial period (dominant size) of structure between 2 areas is 0.1 nm . The thickness of the sample is about $4.5\text{ }\mu\text{m}$, the lateral dimensions $17 \times$

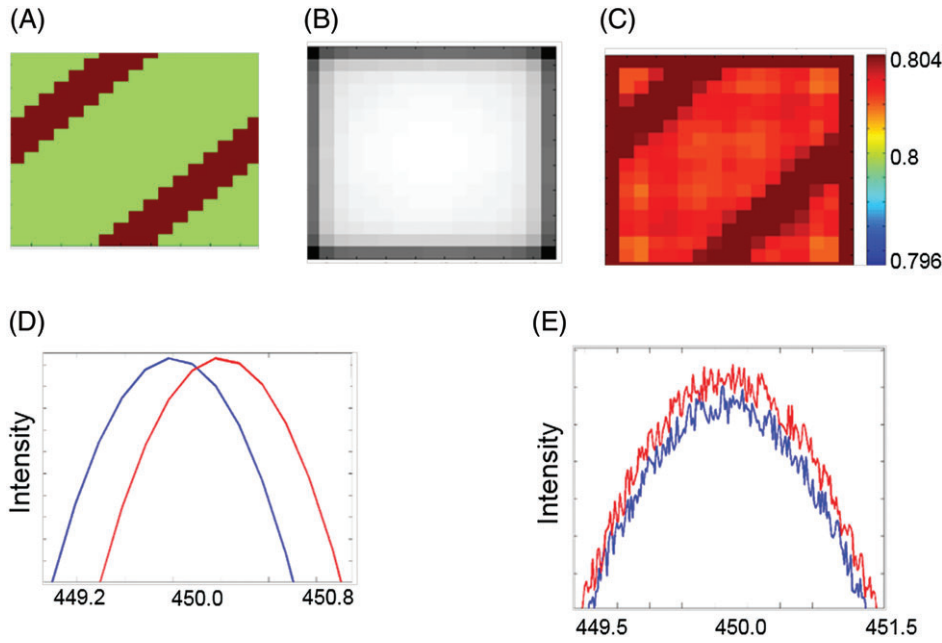


FIGURE 2 Simulation imaging of areas with different structure. (A) an object with 2 areas with different structure (0.1 nm difference), (B) conventional image, (C) sSESF image, (D) axial spatial period profiles at 2 areas in the object with different structure, (E) corresponding axial spatial period profiles in the image plane, line with blue color corresponds to 449.9 nm and with red color corresponds to 450 nm spatial period of the structure

17 microns and the refractive index 1.4. The spectral range of the illumination was 1230–1370 nm. The complex amplitude of the reflected light wave from such sample can be described as a superposition of light scattered from all scatterers along the depth:

$$U(\lambda) = \sum_{m=1}^M U_0 R (1-R)^{2(m-1)} e^{-i[\phi + d\phi(\lambda)(m-1)]} \quad (1)$$

where R is the reflection coefficient; M is a number of scatterers within the sample; $d\phi$ is the phase difference after double passing 1 period of the structure $d\phi = \frac{4\pi dn}{\lambda}$, d , distance between scatterers (spatial period), n , refractive index, λ , wavelength. The corresponding intensity can be written as

$$I_s(\lambda) = U(\lambda)U(\lambda)^* \quad (2)$$

where $U(\lambda)^*$ is a complex conjugate value. This formula describes the intensity of scattered light from each lateral pixel, or point on the surface. Using this, the lateral profiles of intensity of the scattered light were calculated in the sample (object) plane.

The images were formed as a convolution of the light wave scattered from the sample with the point spread function (PSF) of the imaging system. Briefly, for diffraction limited optical system with a circular aperture, the PSF is given by the squared modulus of the Fourier transform of the circular aperture, and can be represented as.

$$h(\theta) = \frac{2J_1(kr \sin(\theta))}{kr \sin(\theta)} \quad (3)$$

where J_1 is the Bessel function of the first kind, r is the aperture radius, θ is the angle of observation and k is the wavenumber. The lateral profiles of intensity of the scattered light were convolved with the PSF of the numerically

simulated imaging system to give the lateral intensity distribution in the image plane and form 2D image. The numerical aperture (NA) of the imaging system is $NA = 0.5$. The central wavelength of illumination is 1300 nm, so the diffraction limited spatial resolution of the imaging system is about 1.6 μm . Conventional images were formed as a superposition of the light waves for all wavelengths. A linear array of detectors was simulated for recoding the resulting intensity spectrum, replicating an imaging spectrometer or swept light source.

To form sSESF images the wavelengths were converted to spatial periods according to the relationship between wavelength and spatial period H_z in k -space (see, for example, formula (22) in Ref. [20]). After convolution with the PSF of the imaging system and conversion in spatial periods for each wavelength, the axial spatial period profiles at each lateral point within the image were reconstructed. The sSESF images were formed as correlation maps between the axial spatial period profile (intensity vs spatial period) of the numerically synthesized structure and axial spatial period profiles at all image points. The relatively large intensity noise was added to simulate real imaging conditions, signal to noise ratio $SNR = 57$ dB.

Numerical structure to probe the sample was synthesized similar to the simulated sample. Any structure can be simulated and used as a probing structure. To better demonstrate the principles of the sSESF approach the same number of scatterers to generate the synthesized structure was used and the spatial period between them was varied to simulate different sizes of the probing structure. The first 2 videos (Videos S1 and S2, Supporting information) present the changes in the axial spatial period profile of the probing structure and in the correlation coefficient at each image point vs changes in size of probing structure. The size of probing structure is changed from 449.5 to 450.4 nm

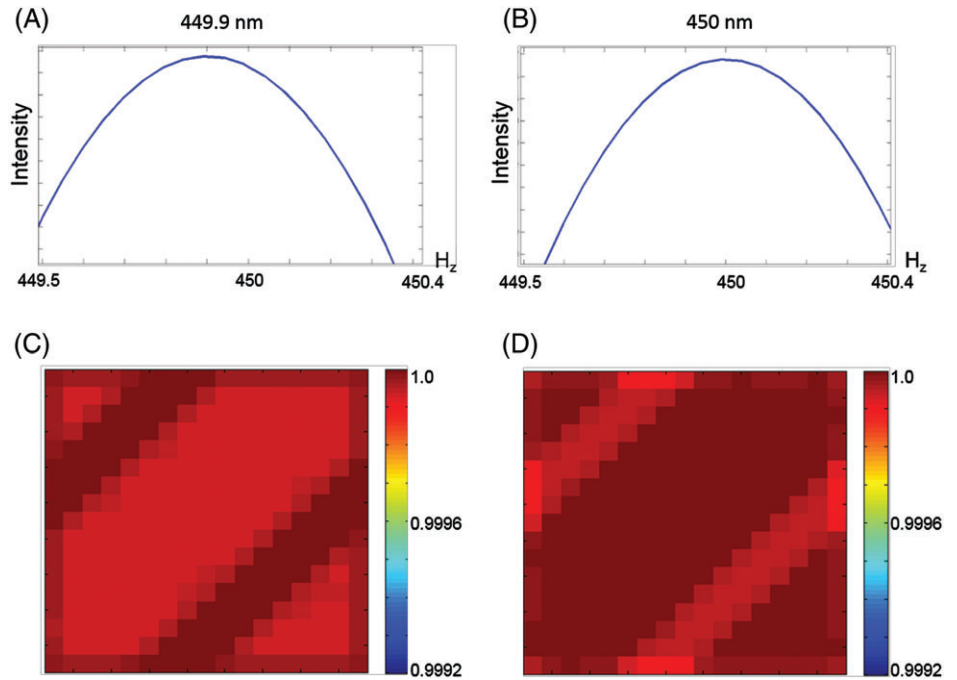


FIGURE 3 Visualization of the sample's structure for 2 sizes of probing structure: (A) and (B) axial spatial period profiles of the probing structure, (C) and (D) the corresponding sSESF images as maps of the correlation coefficient. (for other sizes of probing structure see Videos S1 and S2)

with step 0.02 nm. In Figure 3A,B the 2 frames from this video as an examples of the profiles of probing structure for 2 spatial periods of 449.9 and 450 nm are presented. Corresponding sSESF images are presented in Figure 3C,D.

The samples in Figures 4 and 5 were synthesized and corresponding images were formed using the same methodology described above. The sample in Figure 4A,D consists of 4 repeated areas with different axial structure. There are 20 scatterers along depth and the difference in the axial periods of the structures is 10 nm. The lateral size of each area is 440×440 nm. The whole sample's lateral dimension is about 115×115 μm .

The sample in Figure 5 also consists of 4 repeated areas with different axial structure. There are 40 scatterers along depth and the difference in the axial periods of the structures is 10 nm. The lateral size of each area in the sample is $600 \times$

600 nm. The sample's lateral dimension 153×153 μm . To simulate different sizes of the probing structure we varied the spatial period of the structure from 450 to 480 nm with step 10 nm. Images were formed as maps of correlation coefficient between axial spatial frequency profile of the probing structure and axial spatial frequency profiles of the structure at each pixel in the sample after convolution with the PSF of the imaging system, as before. Noise was also added to simulate real imaging conditions, with SNR of 71 dB.

The numerical structure to probe experimental samples was synthesized using the same methodology. The size of probing structure is changed from 40 to 1000 nm with step 30 nm.

2.3 | Experimental setup

A custom built scanning microscope, described elsewhere, was used for experiments [22]. A light source was a

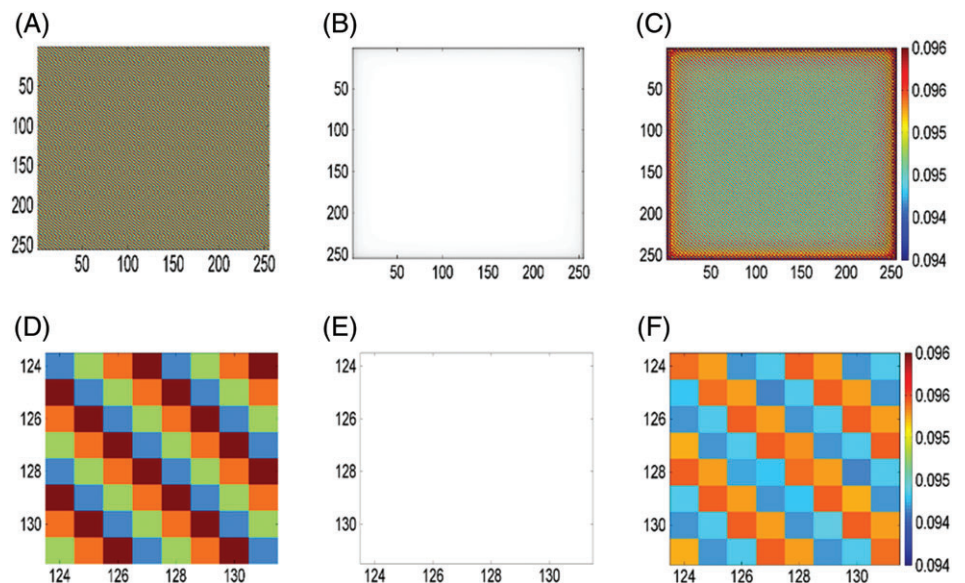


FIGURE 4 Super-resolution sSESF imaging: (A) the sample, (B) a conventional image, (C) sSESF image. (D, E, F) magnified portions of (A, B, C), respectively

broadband superluminescent diode, wavelength range 1230 to 1370 nm. A pair of galvanometric driven mirrors was used for x - y scanning and samples were imaged with an objective lens with $NA = 0.5$. The registration was done using spectrometer consisted of a 50 mm focal length collimator, a 1145 lines/mm transmitting grating, an achromatic lens with a 100 mm focal length and a 14-bit, 1024 pixels InGaAs line scan camera (SU1024LDH2, Goodrich Ltd., Houston, Texas) with a maximum acquisition rate of 91 kHz, spectral resolution 0.14 nm.

2.4 | Samples

To experimentally demonstrate sensitivity to small structural changes and improvement in resolution the samples with nanosphere aggregates of different sizes were made. The polymer spheres from Bangs Laboratories, Inc. with diameters 400, 520 and 620 nm were used to make the samples. An aliquot of about 10 μ L of diluted monodispersed polystyrene nanosphere suspension ($n = 1.59$) was smeared uniformly onto a glass slide and dried, forming nanosphere aggregates.

To demonstrate application of our approach to biomedical samples we investigated the structural changes in collagen tissue vs days of culture. For preparation of 3D collagen-based tissue-engineering scaffolds C2C12 cells (ATCC CRL-1772) were plated in Dulbecco's modified Eagle's medium (DMEM) supplemented with 10% fetal bovine serum (FBS), 100 units/mL penicillin and 100 mg/mL streptomycin at 37°C. Cells were grown to approximately 70%-80% confluence and used for the experiments. Collagen type I was extracted from rat tails and processed as described elsewhere [35]. Briefly, 1 g of air-dried and ultraviolet-sterilized collagen type I tendons extracted from rat tails were solubilized in 300 mL 0.1% acetic acid, obtaining a collagen acid solution at a concentration of 2 mg/mL, as quantified with BCA assay. Collagen gels were then processed by mixing the sterile solution with a suspension of C2C12 murine myoblast (2×10^6). Collagen acidity was neutralized with NaOH (1 M) and NaHCO_3 (0.26 M). This solution was then poured into a mold to obtain vessel-like scaffolds. After 24 h at 37°C the collagen acid solution was jellified in the tube, with cells trapped within, and DMEM 10% FBS was placed as nutrient supplement for the cells (all from Lonza, Belgium). Three samples were kept in a static condition after 3, 7 and 21 days of culture, respectively. After that pieces of collagen tissues, fixed in formaldehyde 4% water solution, were placed in a small dish and images were taken.

Small angle X rays scattering (SAXS) was performed to enable a structural analysis of the matrices at the nanoscale, comparing the scaffolds with the native blood vessels [36]. A Fr-E+ SuperBright rotating copper anode microsource (Cu $K\alpha$, $\lambda = 0.15405$ nm, 2475 W) was focused by a multi-layer focusing optics (Confocal Max-Flux; CMF 15-105) to

a SAXS 3-pinholes camera (Rigaku Matsubara-cho, Akishima-shi, Tokyo, Japan, SMAX-3000). The system was equipped with a Triton 20 gas-filled proportional counter (1024×1024 array, 195 μ m pixel size) for SAXS acquisition, placed at a sample-detector distance of around 2200 mm. This distance give access to a range of scattering vector moduli ($q = 4\pi\sin\theta/\lambda$, where θ is half the scattering angle) of about 0.006 to 0.2 \AA^{-1} . A detailed description of the instrument performances can be found in Ref. [37].

3 | RESULTS

3.1 | Numerical simulation

Results of numerical simulation of the imaging of the sample which consists of 2 areas with different structure is presented in Figure 2. In the conventional image, Figure 2B,

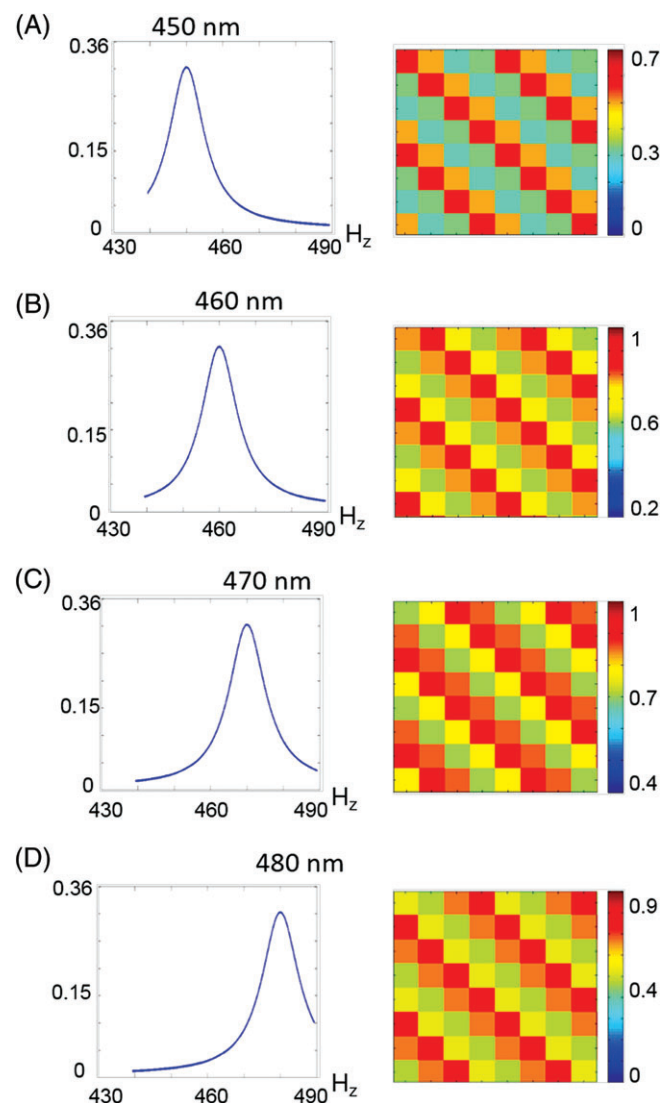


FIGURE 5 Probing structure within a super-resolution image. (A), (B), (C) and (D) profiles of probing structure and corresponding sSESF images for spatial periods of probing structure 450, 460, 470 and 480 nm, respectively

areas with different structure cannot be detected, but in the sSESF image in Figure 2C, formed as a correlation between probing numerically synthesized structure and the sample's structure, these areas can be clearly seen. So the difference in size of structure of just 0.1 nm can be detected using sSESF approach. Visualization of these areas is possible because the difference between the axial spatial period profiles for the 2 areas, Figure 2D, can be detected in the image plane, even at a SNR of 57 dB, as seen in Figure 2E.

In Figure 3A,B the axial period profiles of probing structures with 2 different sizes are presented. The correlation coefficient in Figure 3C,D is constant within 2 lines and another correlation coefficient is constant within other area in the image. It can be seen that for a size of probing structure of 449.9 nm, the maximum correlation is within 2 lines in the sSESF image in Figure 3C, but for size of probing structure 450 nm, the maximum correlation is within other area in the SESF image in Figure 3D. So, by probing the sample using different sizes of numerically synthesized structure, it is possible not just to visualize areas with different structures within the sample, but also perform some quantitative estimation of the structures.

The technique also permits the formation of super-resolution images. Images of the sample presented in Figure 4A,D were formed using the same virtual imaging system as before. Conventional and super-resolution sSESF images are presented in Figure 4B,C correspondingly. In Figure 4D-F the magnified portions of the images in Figure 4A-C are presented.

In the conventional image, Figure 4B,E, it is impossible to resolve areas with different structure, as the size of each area is more than 3 times smaller than the resolution limit of the imaging system. But in the sSESF image, Figure 4C, F, all areas with different structure are clearly resolved.

Using the proposed method, it is also possible to perform quantitative estimation of the structure within areas smaller than the diffraction resolution limit. In Figure 5 it is shown that when different sizes of probing structure are used, the corresponding areas within the sample which better correlate with the given size or spatial profile of the probing structure, are visualized. The size of each area is 600×600 nm, which is more than 2 times smaller than the resolution limit of the optical system. In Figure 5A-D the structure at areas in red have maximum correlation with the probing structure, so the structure at these areas is similar to the probing structure. For example, in Figure 5A the areas with size corresponding to 450 nm size of probing structure are visualized, in Figure 5B—with size corresponding to 460 nm size of probing structure, and so on.

3.2 | Experimental results

For our experiments, we used a scanning microscope described in Experimental section. The imaging system, the spectral bandwidth of illumination, and the central

wavelength were the same as we used for the numerical simulation. Initially, imaging of polystyrene sphere aggregates of different sizes was performed. In Figure 6, conventional images (A, B, C), and the corresponding SESF images, formed as mean spatial frequency (D, E, F), and as maps of correlation coefficient at a period of probing structure 400 nm (sSESF images) (G, H, I), are presented. The size of all the images in Figure 6 is $11 \times 11 \mu\text{m}$. It is impossible to get any information about the structure from the conventional images, (A, B, C). From the SESF images (D, E, F), formed as a maps of the mean spatial frequency, it can be seen that the mean spatial period of the dominant structure increased when the size of the spheres increased.

Averaged over the image, the mean spatial period for the sample with 400 nm spheres is 407 nm, for the sample with 520 nm spheres it is 409 nm, and for the sample with 620 nm spheres it is 410 nm. From these images one can make the conclusion that the dominant size of the structure in Figure 6E) is larger than that in Figure 6D, and the dominant size of the structure in Figure 6F is larger than in Figure 6E. From the sSESF images, Figure 6G-I, it is also possible to detect samples with different structure: the average correlation coefficient decreases when the size of the spheres increases in comparison with 400 nm spheres. The corresponding averaged correlation coefficients for samples with spheres 400, 520 and 620 nm are 0.74, 0.66 and 0.62, respectively. Differences in size of structure within the different samples, which is just about 100 nm, can be clearly seen from the plot of averaged along the sample correlation coefficient vs different size of probing structure, as presented in Figure 6J.

As was shown by numerical simulation, by using our method it is possible to visualize structure within areas smaller than the resolution limit. The size of the imaged area in Figure 7 approximately corresponds to the resolution limit of the imaging system. So in the conventional image, Figure 7A, areas with different structure are unresolvable. In the sSESF image, Figure 7B, formed as a map of correlation with a numerically synthesized structure, areas with approximately similar internal structure (which corresponds to 4 spheres), separated by small gaps with different structure, are clearly visualized.

In next experiment we applied our approach to study the structure of 3D collagen-based tissue-engineering scaffolds, processed as previously described, vs number of days of culture. Different modalities of the SESF images of the collagen scaffolds are presented in Figure 8. The size of all images is $11 \times 11 \mu\text{m}$. Three samples were kept in a static condition after 3, 7 and 21 days of culture, respectively. From the SESF images (A, B, C), formed as maps of the spatial period at maximal signal, it can be seen that the structure of collagen tissue vs number of days of culture becomes more uniform, and the range of variations of the spatial period of the dominant structure is reduced.

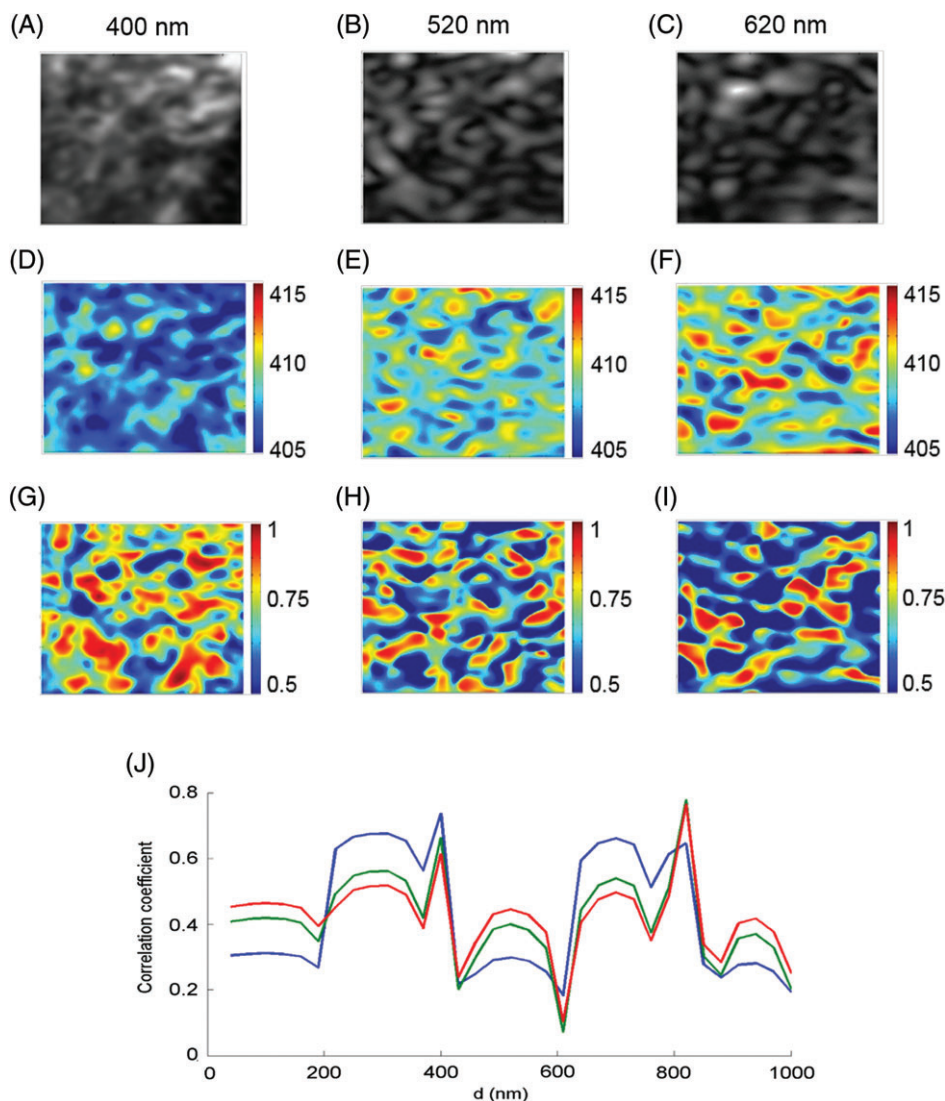


FIGURE 6 Images of polystyrene sphere aggregates of different sizes. (A, B, C) conventional images of spheres with diameters 400, 520 and 620 nm. (D, E, F) corresponding SESF images of mean spatial frequency. (G, H, I) sSESF images as maps of the correlation coefficient for a period of probing structure 400 nm (for other sizes of probing structure see Supporting Information, Videos S3-S5). (J) averaged correlation vs different sizes of probing structure, blue for 400 nm spheres, green for 520 nm spheres and red for 620 nm spheres

The same conclusion can be made from analysis of the SESF images (D, E, F), formed as maps of mean spatial period, and from the sSESF images (G, H, I), formed as correlation coefficient distributions between spatial period profile of numerically synthesized structure and spatial period profiles of the sample's structure. The range of correlation coefficients over the samples is reduced vs number of

days of culture. The mean size of the structure remains approximately constant for all numbers of days of culture, as can be seen from the plot of averaged correlation vs different sizes of probing structure from 40 to 1000 nm, formed for 3, 7 and 21 days of culture.

Small angle X rays scattering (SAXS) were performed to enable a structural analysis of the matrices at the nano-scale, comparing the scaffolds with the native blood vessels. SAXS 1D profiles after background subtraction and deconvolution [38], shown in Figure 9, were collected from collagen scaffolds, maintained in culture for 3, 7 and 21 days, and from the reference model of native aorta. The qualitative comparison with a native aorta, used as reference model, shows the structural similarity between the reference model and the collagen-based scaffolds. The number in the upper side of the Figure 9 indicate the diffraction orders.

The result was also quantitatively confirmed by the evaluation of the correlation coefficient between each profile from the collagen scaffolds and the SAXS profile of the porcine aorta vessel as reported in Figure 9. The highest degree of similarity with native porcine aorta model is

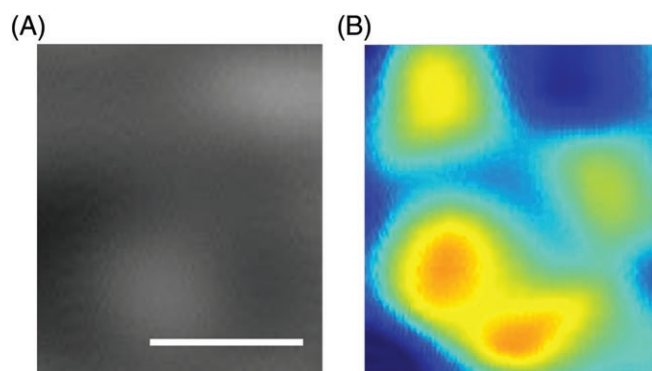


FIGURE 7 Images of 400 nm diameter spheres. (A) conventional image, (B) sSESF image. The scale bar is 1 μm

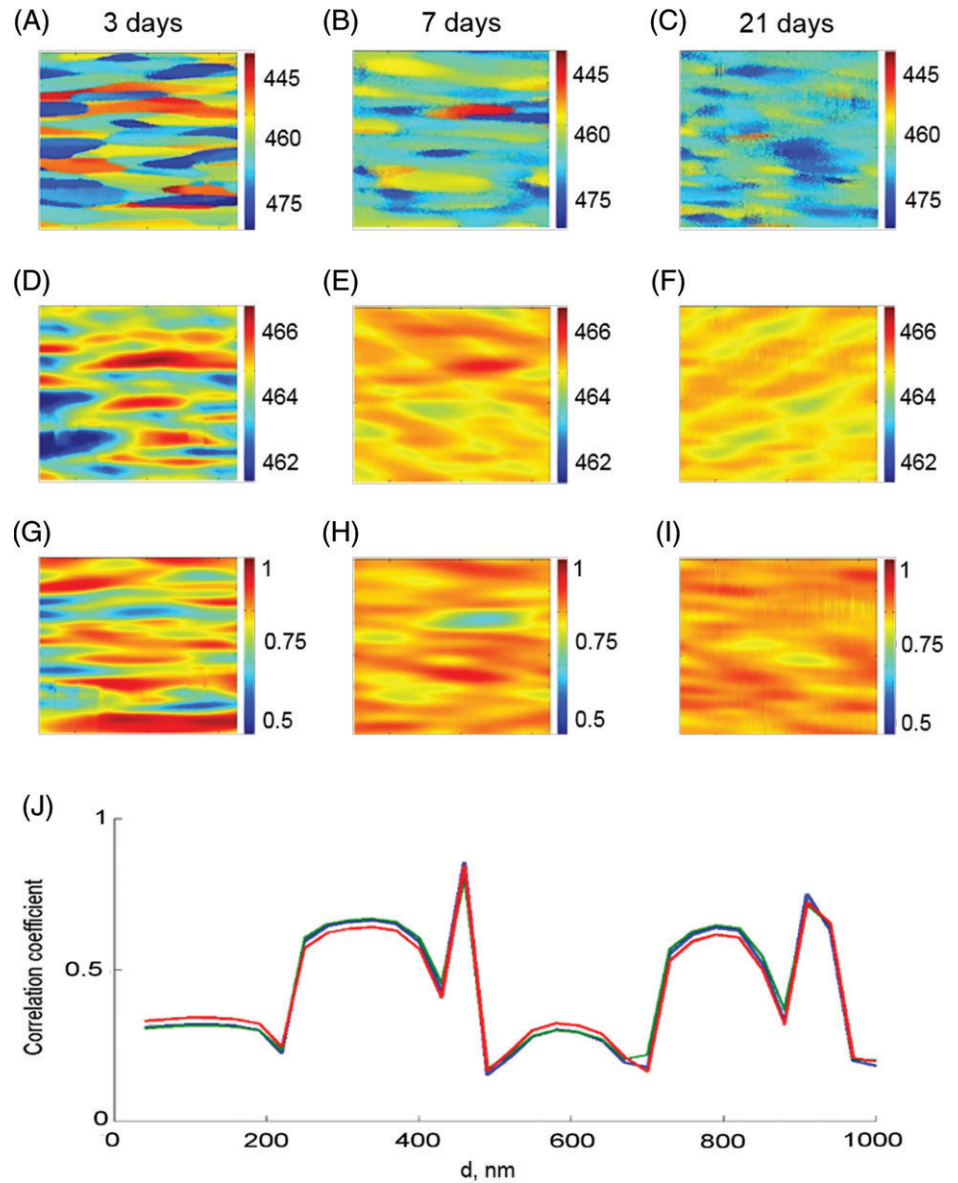


FIGURE 8 Imaging of the collagen scaffolds as a function of the day of culture. (A, B, C) SESF images as maps of the spatial period at the maximal signal distributions. (D, E, F) SESF images as maps of mean spatial period. (G, H, I) sSESF images as maps of the correlation coefficient distributions (for other sizes of probing structure see Videos S6-S8). (J) Averaged correlation coefficients vs size of probing structure, green for 3 days, of culture red for 7 days and blue for 21 days

observed at the longest culturing time (21 days). Moreover the results obtained by the sSESF images were also confirmed by the SEM analysis on the sample that show a collagen matrix consisting of thin uniform collagen fibrils at the highest culture time [36].

4 | DISCUSSION

The proposed new approach, sSESF microscopy, provides sub-nano sensitivity to structural changes, quantitative estimation of the structure at different locations, the possibility to probe structure using different sizes of the numerically synthesized structure after recording just 1 single image, detection the areas within the sample with given structure (some similarity with Fourier spatial filtering, but more powerful method), the possibility to compare structure within areas which are smaller than the diffraction resolution limit of the optical system, quantitative comparison of

the structure of different samples. Such unique features give significant additional advantages beyond the super-resolution imaging we reported previously [22].

The results of the numerical simulations in Figures 2 and 3 demonstrate the sub-nano sensitivity to structural changes. Even in the presence of noise, a difference in structure of 0.1 nm can be detected. Usually intensity-based images where at each image point we have just 1 intensity value suffer from intensity noise; variations in intensity suppress spatial resolution. In contrast, in our method at each image point we have axial spatial frequency profiles, so many values, and each of them is detected by corresponding pixel of the multielement array detector (CCD or CMOS camera). This situation has some similarity with comparison between time domain and Fourier domain optical coherence tomography (TDOCT and FDOCT). For example, it was shown that replacement of the single-element detector with a multielement array detector significantly reduces the short noise [39, 40]. In conventional microscopy where intensity

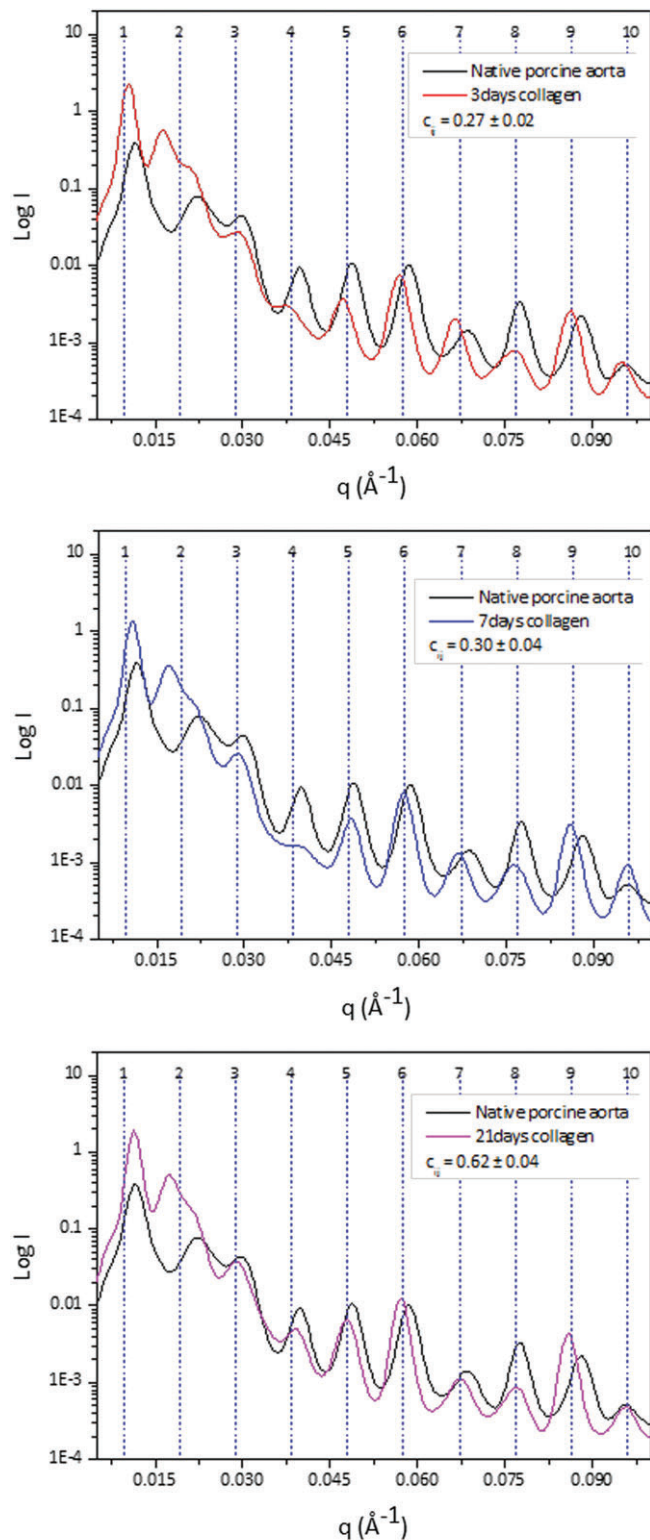


FIGURE 9 1D SAXS profiles comparison between the collagen scaffolds and the native porcine vessels. C_{ij} indicates the correlation coefficient between porcine vessel and collagen scaffolds diffraction patterns at different days of culture

at each image point is detected by single-element detector or single pixel of the detector the shot noise generated by the power density at 1 specific wavelength is also present at all other wavelengths. In SESF approach at each image

pixel we have spectrum, detected using spectral device (imaging spectrometer), including multielement array detector. Each wavelength and corresponding spatial frequency is detected by separate detector and the cross shot-noise term is eliminated. If the thickness of the sample and the corresponding number of scatterers were to be increased, then the sensitivity would be further improved.

The improvement in resolution, demonstrated by numerical simulation and experimentally, can be explained by the significantly enhanced information content of the image as it is described in the Methods. Instead of just 1 intensity value at each image point, as in conventional microscopy, we have hundreds or even thousands of values. As a result, areas with different structure can be visualized, even if their size and the distance between them are smaller than the resolution limit. Increasing the spectral bandwidth of illumination would increase the range of detected spatial frequencies at each location, and so improve the information content of the image that could lead to improvement in sensitivity to structural alterations and resolution. Comparison of axial spatial frequency profiles with profiles of synthesized structure provides flexibility for probing the structure within the object and permits quantitative information to be obtained. We showed that from a single image it is possible to get information about structural content within different areas of the sample by probing the image with different sizes of the synthesized structure. Figure 3, Figure 6G-J, Figure 8G-J and Videos S1 and S2, S3-S5, and S6-S8, which are impossible to get using known techniques, demonstrate that. This operation has some analogy with 2D spatial Fourier filtering. In 2D spatial Fourier filtering the areas within the sample which correspond to selected lateral spatial frequencies are visualized. Using sSESF approach it is possible to probe the sample using axial spatial frequency profile either numerically synthesized structure or taking such profile from real structure. Then the areas within the sample which have structures similar to the probing structure, will be visualized. But beside that it is possible to see how close the structure in other areas to probing structure. The size of these areas, as it was demonstrated in the paper, can be even smaller than resolution limit of the imaging system. So sSESF approach is more powerful and has obvious advantages in comparison with conventional 2D Fourier filtering. This makes the technique promising for visualization and study of different pathological areas within the biological tissues.

Analysis of correlation for specific areas vs the size of the probing structure can help to differentiate local and averaged sizes of structure between different samples or areas within the sample. For example, a difference in size of spheres of about 100 nm, which is more than 10 times smaller than diffraction resolution limit of the imaging system, can be clearly seen from Figure 6J.

A similar plot in Figure 8J, formed for collagen scaffolds of 3, 7 and 21 days of culture, does not show a difference in averaged along the sample sizes of structure. At the same time, SESF and sSESF images in Figure 8 suggest that structure becomes more uniform vs days of culture. The result, obtained using this label-free optical technique in far field, was confirmed by X-ray scattering microscopy measurements. A possible reason for such structural alterations without changing of the average size could be straightening of the collagen fibers vs time which is related to cell spreading into the matrix and to extracellular matrix remodeling normally performed by cells.

This finding demonstrates potential and significance of the new technique for study of biological objects. Collagen fiber orientation and uniformity highly influence tissue mechanical properties. In fact, the complex structure provides fibrillar structures with features suited for both their roles as biomechanical tensile materials and as a source of intermolecular connectivity. The ubiquity of collagen in most animal tissues shows that a high degree of functionality can be joined by modulations on a relatively stable framework. Different microstructures normally subtend different crosslinking degrees, which are finely related to tissues biomechanical characteristics. In a standard stress-strain curve of a collagenous tissue, cross-linking results in an increase in breaking strength and stiffness. Correlating the microstructure with the physical-chemical characteristics of collagen matrices is of high interest in tissue engineering and regenerative medicine.

The hierarchical organization of collagen-based materials from the molecular to the functional tissue allows matrices to be obtained with optimized biomechanical properties for several applications such as skin regeneration, as well as for osteo-articular renewal (ie, tendons, ligaments, cartilage).

Cells are continuously modifying their own environment by way of extracellular matrix protein synthesis and degradation. This physiologically helps to maintain the optimal functional conditions in terms of biological and mechanical properties of the tissues. Such process is normally named "tissue homeostasis." Every change which alters this balance leads to pathological conditions. Studying the cellular behavior over time helps to better understand how a 3-dimensional environment (native or artificial) may influence the biological response and, vice versa, how an altered cellular environment modifies the surrounding matrices.

5 | CONCLUSION

A novel label-free method for visualization and study of structure at the nanoscale is presented. The main steps include reconstruction of the axial spatial frequency/period profiles for each point in the image, formation of a probing structure (numerically or using the structure of some

sample) and image formation as a correlation map between the object's structure and the probing structure. Sub-nano sensitivity to structural changes and super-resolution imaging has been demonstrated by numerical simulation. It has been shown that areas with specific structure within the sample can be visualized by probing using corresponding numerically synthesized structure. Even if sizes of these areas are smaller than resolution limit of the imaging system and difference in structural sizes is at nanoscale, such areas can be detected. Experimental results confirm the unique abilities of the proposed method, and demonstrate advantages in comparison with conventional microscopy techniques. The method can be adapted to different specific areas of applications. For example, application could be investigation of the sub cellular structure where the high resolution version should be used. Other possible application is imaging of relatively large (say cm scale) areas of biological tissue with nano-sensitivity to detect pathological areas. For this application the specially designed low resolution imaging system should be used. Possible areas of application of the sSESF imaging include biomedical science, material science, chemistry, nanotechnology, etc.

ACKNOWLEDGMENTS

This work was supported by NUI Galway, Galway University Foundation, the University of Limerick Foundation, the National Biophotonics Imaging Platform (NBIP) Ireland funded under the Higher Education Authority PRTLI Cycle 4, co-funded by the Irish Government and the European Union—Investing in your future, and Compact Imaging, Inc. S.A., J.G., H.S., J.H. and M.L. have a financial interest in Compact Imaging, Inc.

AUTHOR BIOGRAPHIES

Please see Supporting Information online.

REFERENCES

- [1] S. A. Alexandrov, T. R. Hillman, T. Gutzler, D. D. Sampson, *Phys. Rev. Lett.* **2006**, 97, 168102.
- [2] J. Morrison, L. Raty, P. Marriotti, P. O'Toole, *Sci. Rep.* **2013**, 3, 2369.
- [3] V. Mico, Z. Zalevsky, C. Ferreira, J. Garcia, *Opt. Express* **2008**, 16, 19260.
- [4] T. R. Hillman, T. Gutzler, S. A. Alexandrov, D. D. Sampson, *Opt. Express* **2009**, 17, 7873.
- [5] L. Li, W. Guo, Y. Z. Yan, S. Lee, T. Wang, *Light-Sci. Appl.* **2013**, 2, e104.
- [6] I. Pita, N. Hendaoui, N. Liu, M. Kumbham, S. A. M. Tofail, A. Peremans, C. Silien, *Opt. Express* **2013**, 21, 25632. <https://doi.org/10.1364/OE.21.025632>.
- [7] E. G. van Putten, D. Akbulut, J. Bertolotti, W. L. Vos, A. Lagendijk, A. P. Mosk, *Phys. Rev. Lett.* **2011**, 106, 193905.
- [8] P. Wang, M. N. Slipchenko, J. Mitchell, C. Yang, E. O. Potma, X. F. Xu, J. X. Cheng, *Nat. Photonics* **2013**, 7, 450.
- [9] P. von Olshausen, A. Rohrbach, *Opt. Lett.* **2013**, 38, 4066.

- [10] L. Cherkezzyan, I. Capoglu, H. Subramanian, J. D. Rogers, D. Damania, A. Taflove, V. Backman, *Phys. Rev. Lett.* **2013**, *111*, 033903.
- [11] I. Itzkan, L. Qiu, H. Fang, M. M. Zaman, E. Vitkin, L. C. Ghiran, S. Salahuddin, M. Modell, C. Andersson, L. M. Kimerer, P. B. Cipolloni, K. H. Lim, S. D. Freedman, I. Bigio, B. P. Sachs, E. B. Hanlon, L. T. Perelman, *Proc. Natl. Acad. Sci.* **2007**, *104*, 17255.
- [12] J. E. Chandler, L. Cherkezzyan, H. Subramanian, V. Backman, *Biomed. Opt. Express* **2016**, *7*, 883.
- [13] R. K. Bista, S. Uttam, P. Wang, K. Staton, S. Choi, C. J. Bakkenist, D. J. Hartman, R. E. Brand, Y. Liu, *J. Biomed. Opt.* **2011**, *16*, 070503.
- [14] S. Uttam, R. K. Bista, K. Staton, S. Alexandrov, S. Choi, C. J. Bakkenist, D. J. Hartman, R. E. Brand, Y. Liu, *Biomed. Opt. Express* **2013**, *4*, 2491.
- [15] A. K. Ellerbee, T. L. Creazzo, J. A. Izatt, *Opt. Express* **2007**, *15*, 8115.
- [16] M. G. Shan, M. E. Kandel, G. Popescu, *Opt. Express* **2017**, *25*, 1573.
- [17] S. A. Alexandrov, S. Uttam, R. K. Bista, Y. Liu, *Opt. Lett.* **2011**, *36*, 3323.
- [18] S. A. Alexandrov, S. Uttam, R. K. Bista, C. Q. Zhao, Y. Liu, *Opt. Express* **2012**, *20*, 9203.
- [19] S. A. Alexandrov, S. Uttam, R. K. Bista, K. Staton, Y. Liu, *Appl. Phys. Lett.* **2012**, *101*, 033702.
- [20] S. Uttam, S. A. Alexandrov, R. K. Bista, Y. Liu, *Opt. Express* **2013**, *21*, 7488.
- [21] S. A. Alexandrov, H. M. Subhash, A. Zam, M. Leahy, *Nanoscale* **2014**, *6*, 3545.
- [22] S. A. Alexandrov, J. McGrath, H. Subhash, F. Boccafroschi, C. Giannini, M. Leahy, *Sci. Rep.* **2015**, *5*, 13274.
- [23] W. Lukosz, *J. Opt. Soc. Am.* **1967**, *57*, 932.
- [24] G. Toraldo di Francia, *J. Opt. Soc. Am.* **1969**, *59*, 799.
- [25] I. J. Cox, C. J. R. Sheppard, *J. Opt. Soc. Am. A-Optics Image Sci. Vis.* **1986**, *3*, 1152.
- [26] A. L. Kartashov, *Opt. Spectrosc.* **1960**, *9*, 204.
- [27] S. A. Basinger, E. Michielssen, D. J. Brady, *J. Opt. Soc. Am. A-Optics Image Sci. Vis.* **1995**, *12*, 704.
- [28] A. M. van Oijen, J. Kohler, J. Schmidt, M. Muller, G. J. Brakenhoff, *Chem. Phys. Lett.* **1998**, *292*, 183.
- [29] M. Davidson, K. Kaufman, I. Mazon, F. Cohen, *Proc. SPIE* **1987**, *775*, 233.
- [30] G. Hausler, M. W. Lindner, *J. Biomed. Opt.* **1998**, *3*, 21.
- [31] C. J. R. Sheppard, K. G. Larkin, *Appl. Opt.* **1995**, *34*, 4731.
- [32] T. S. Ralston, D. L. Marks, P. S. Carney, S. A. Boppart, *Nat. Phys.* **2007**, *3*, 129.
- [33] C. J. R. Sheppard, S. S. Kou, C. Depeursinge, *J. Opt. Soc. Am. A-Optics Image Sci. Vis.* **2012**, *29*, 244.
- [34] M. Born, E. Wolf, *Principles of Optics*, Cambridge University Press, Cambridge **1999**, p. 695.
- [35] N. Rajan, J. Habermehl, M. F. Cote, C. J. Doillon, D. Mantovani, *Nat. Protoc.* **2006**, *1*, 2753.
- [36] F. Boccafroschi, M. Ramella, T. Sibillano, L. De Caro, C. Giannini, R. Comparelli, A. Bandiera, M. Cannas, *J. Biomed. Mater. Res. A* **2015**, *103*, 1218.
- [37] D. Altamura, R. Lassandro, F. A. Vittoria, L. De Caro, D. Siliqi, M. Ladisa, C. Giannini, *J. Appl. Crystallogr.* **2012**, *45*, 869.
- [38] T. Sibillano, L. De Caro, D. Altamura, D. Siliqi, M. Ramella, F. Boccafroschi, G. Ciasca, G. Campi, L. Tirinato, E. Di Fabrizio, C. Giannini, *Sci. Rep.* **2014**, *4*, 6985.
- [39] J. F. de Boer, B. Cense, B. H. Park, M. C. Pierce, G. J. Tearney, B. E. Bouma, *Opt. Lett.* **2003**, *28*, 2067.
- [40] R. Leitgeb, C. K. Hitzenberger, A. F. Fercher, *Opt. Express* **2003**, *11*, 889.

SUPPORTING INFORMATION

Additional supporting information may be found online in the Supporting Information section at the end of the article.

Appendix S1. Supporting Information.

Appendix S2. Author biography.

Video S1. Changes in size of probing structure which is used to probe a numerically synthesised object presented in Fig. 2A.

Video S2. Changes in sSESF image of the numerically synthesized object as a result of probing with numerically synthesized structure (Video S1).

Video S3. Changes in sSESF image of 400 nm spheres aggregates as a result of probing with numerically synthesized structure.

Video S4. Changes in sSESF image of 520 nm spheres aggregates as a result of probing with numerically synthesized structure.

Video S5. Changes in sSESF image of 620 nm spheres aggregates as a result of probing with numerically synthesized structure.

Video S6. Changes in sSESF image of the collagen scaffold at 3 days of culture as a result of probing with numerically synthesized structure.

Video S7. Changes in sSESF image of the collagen scaffold at 7 days of culture as a result of probing with numerically synthesized structure.

Video S8. Changes in sSESF image of the collagen scaffold at 21 days of culture as a result of probing with numerically synthesized structure.

How to cite this article: Alexandrov S, McGrath J, Sheppard CJR, et al. Label-free ultra-sensitive visualization of structure below the diffraction resolution limit. *J. Biophotonics*. 2018;e201700385. <https://doi.org/10.1002/jbio.201700385>